PNAS nexus

PNAS Nexus, 2022, **1**, 1–10
https://doi.org/10.1093/pnasnexus/pgac161
Advance access publication date: 18 August 2022
Research Report

A shrinkage-based criterion for evaluating resistance spot weldability of alloyed steels

Shuoshuo Li[a,b], Yanjun Wang[c], Bin Hu[a,b], Wu Tao[c], Shanglu Yang[c,d,*] and Haiwen Luo[a,b,*]

[a]State Key Laboratory of Advanced Metallurgy, University of Science and Technology Beijing, Beijing 100083, China
[b]Department of Ferrous Metallurgy, University of Science and Technology Beijing, Beijing 100083, China
[c]Shanghai Institute of Optics and Fine Mechanics, Chinese Academy of Sciences, Shanghai 201800, China
[d]Center of Materials Science and Optoelectronics Engineering, University of Chinese Academy of Sciences, Beijing 100049, China
*To whom correspondence should be addressed: Email: yang_unitech@126.com; luohaiwen@ustb.edu.cn
Edited By: Krzysztof Żur.

Abstract

For many decades, several classical formulas on carbon equivalent (CE) have been widely used for evaluating the weldability of steels. Unfortunately, a single CE is impossible for various types of steels. In this study, the resistance spot weldability of medium-Mn steels was investigated. In particular, the influences of paint baking processes at different temperatures on the mechanical properties, fracture mode, and microstructure of weldment were studied. It was found that the paint baking above 170°C can change the tensile-shear failure of weldment from the undesired interfacial failure to the desired pull-out one, because the shrinkage of weldment during welding was compensated by the thermal expansion during the baking, leading to the "cold welding" realized for solid joining. Furthermore, a shrinkage-based criterion (Δl) was established for evaluating the weldability of greater range of alloyed steels more accurately and robustly than CE. The proposed criterion on measuring the weldability of high alloyed steels opens a promising path forward for designing a new generation of advanced high strength steels requiring good weldability.

Keywords: weldability, medium–Mn Steel, resistance spot welding, failure mode, solidification shrinkage

Significance Statement:

We clarify the microstructural mechanism on the interfacial failure of weldment in high alloyed steels, which results from the sufficiently large solidification shrinkage during welding. A baking treatment above 170°C can remove these interspaces between solidified dendrites by the thermal expansion; consequently, many dendrites near the centerline can be mechanically contacted for achieving cold welding, resulting in significantly improved mechanical properties and pull-out failure of weldment. Finally, a new shrinkage-based criterion was established by quantifying shrinkage based on chemistries so that the weldability of greater range of alloyed steels can be assessed more accurately and robustly than the present concept of "carbon equivalent."

Introduction

The development of advanced high strength steels (AHSSs) receives increasing attention from both steel and automotive industries since their application can reduce vehicle weight and increase crashworthiness due to the combination of high strength and good formability (1). However, there exists several challenges on welding AHSSs, including the formation of liquid metal embrittleness (2, 3), weld discontinuities and defects (4), porosities (5, 6), slag (7), and highly pressurized zinc vapor induced spatter (8, 9). All of them may cause the unexpected failure of welded joints. Among the various welding techniques, resistance spot welding (RSW) has been widely used in the automotive industry to assemble the vehicle due to its high flexibility and low cost. It is known that some AHSSs are sensitive to the interfacial failure (IF) due to their special alloying chemistries (10, 11), leading to deteriorated weldability. A typical example is medium-Mn steels (MMS) that usually contain 4–12 wt.% Mn content. Although they are considered as the potential third generation AHSSs due to the excellent combination of ultrahigh strength and high ductility (12–17), they often exhibit a poor weldability. This is presumably due to their high values of carbon equivalent (CE), which is the widely accepted concept in engineering practice for evaluating the weldability of alloyed steels (18). For examples, the IF mode was frequently observed in the tensile-shear (TS) tests for the spot-resistance-welded 5Mn (weight percentage unless stated elsewhere) steel by Jia et al. (19), 7Mn steel by Li et al. (20), and 7 to 9Mn steel by Park et al. (21), who also found that the cross-tension (CT) strength of weldment was inferior to that of conventional TRIP steel with lower CE. In summary, the spot-welded MMSs are frequently subjected to the IF rather than the desired pull-out failure (PF).

To our knowledge, why the TS–IF frequently occurs in the weldment of MMSs remains unclear. In general, the transition from the IF to the PF mode requests the size of weld nugget greater

Competing Interests: The authors declare no competing interest.
Received: April 29, 2022. **Accepted:** August 12, 2022

than the critical value, which is usually realized by increasing the welding current/duration (22, 23). However, it was found that even a heat input during welding was sufficient to cause a serious expulsion but not yet able to produce the expected PF in the weldment of 5Mn steel (19). In our previous research (13), the PF was achieved in the 7Mn–0.14C steel weldment by using the interstitial free steel shims to assist RSW, through which the CE of weld nugget was decreased due to the melt of C-free steel shims merging to weldment. Nevertheless, the actual microstructural mechanism on the IF of MMS weldment has not yet been well understood. Park et al. (21) first proposed that the boundary segregation of high Mn content in 7 and 9Mn steels may promote the formation of brittle martensite, causing the IF of weldments. However, they did not observe the remarkable segregation of Mn at prior austenitic grain boundaries (24). By varying both the cooling time after welding and the postheating pulses, Wang et al. (25, 26) managed to change the IF mode to the partial interfacial failure (PIF) in the CT test of spot welded 7Mn steel, which is because tempered martensite has higher toughness to insist the crack propagation in the nugget. However, why the cracking in a tempered martensite could propagate first along and later perpendicular to the interface was not explained at all. In addition, it was found that the paint baking after RSW can significantly improve the CT strength in the dissimilar MMS/dual phase (DP) steel weldment (24), hinting that the low-temperature tempering of martensite may indeed improve weldability. Nevertheless, the PF could be achieved during the RSW of TRIP steel (27), DP steel (28), and martensitic steel (29, 30) without tempering or baking, i.e. the tempering of martensite in nugget is not necessarily required for improving weldability. Moreover, it was reported that the baking process had the positive effect on the weldability of QP980 steel but no effect on DP980 steel (31). These contradictory results are apparently attributed to the different compositions of studied steels. In summary, a deep insight into the influence of baking on the weldability of different steels is still in lack.

In this study, we report the actual microstructural mechanism on the frequent IF failure in the spot-welded MMS and explain why the paint baking after RSW can significantly improve weldability via quantifying the influences of compositions on the volume change of studied steel during welding. Furthermore, a new model was developed for evaluating the weldability of both low-alloyed and high-alloyed steels, which can effectively predict the transition of IF to PF mode for the steel grades covering a much larger range of alloying contents than those assessed by the "CE," although the latter is still widely used for engineering practice today.

Experimental Procedures

The chemical composition of studied MMS is 7.14Mn–0.14C–0.23Si in weight percentage (termed 7Mn steel), received as the cold-rolled 1.6-mm-thick sheets without coating. The received 7Mn steel sheets were resistance spot welded according to the welding configuration and parameters shown in Fig. S1, in which 16-mm-diameter domed CuCrZr electrodes with a 6 mm face diameter were used. The welding schedule was optimized and adjusted according to the ISO 18278-2:2016 standard. Two steel sheets were welded using a direct current resistance welding machine (OBARA SIV37, FANUC 2000ic-210F, see Fig. S2). Some of welded specimens were subjected to the paint baking at the temperatures ranged from 80 to 250°C for 20 min, termed "baked," while those without baking termed "nonbaked." For comparison, another MMS sheets having the nominal composition of 6.94Mn–0.25C–3.29Cr–0.38Si–0.1(V + Nb) (termed 7Mn–3Cr) and the thickness of 1.5 mm were also spot welded with the same method.

The mechanical behavior of spot welds was evaluated by the TS tests at the crosshead speed of 2 mm/min using a SUNS UTM5105 testing machine according to BS EN ISO 14,323–2015 standard. A minimum of three replicates were tested for each condition. Microhardness was measured using a Vickers hardness tester (BUEHLER 402MVD) at a load of 500 g and a dwell time of 10 s. Nanohardness was examined by using nanoindentation tester (Keysight technologie, G200) at a maximum indentation depth of 100 nm. Moreover, the thermal expansion (change in length) was measured during the heating from 25 to 250°C on the specimen having the dimension of 1.5 × 1.5 × 50 mm by thermal dilatometer (TA, DIL802, USA).

The microstructures were first examined under optical microscope (OM, VHX-6000) after the regular mechanical polishing and then the etching in 4% nital. Both the fracture surfaces and interdendritic space were examined by a scanning electron microscopy (SEM, JSM-6701F). The element analysis was conducted by energy dispersive spectroscopy in SEM. The dendrite morphology was revealed by etching in a saturated aqueous picric acid solution with the addition of sodium alkylsulfonate (32). The foils for transmission electron microscopy (TEM) were first mechanically ground to a thickness of 40 μm and then electro-polished in a solution of 5% perchloric acid and 95% ethanol (vol.%) at around −25°C using twin-jet electropolishing device. TEM examination was performed on the JEM-2200FS, JEOL.

The inner defects in MMS nugget were examined by high-resolution X-ray nano-computed tomography (XCT), EasyTom 160 (RX solutions, France). The samples with 1 mm diameter and 0.9 mm height were cut from the centerline part of both baked and nonbaked nuggets. They were scanned for 5.5 h at a voxel size of 400 nm, using the X-ray tube voltage and the current settings of 100 kV and 60 μA, respectively. A high pixel CCD detector was used to acquire radiographs. Image reconstruction was performed using the XAct CT software (RX Solutions, France). Both the 3D exhibition and the quantitative statistics on the inner defects like porosity are acquired by post analysis.

Results

Influence of paint baking on mechanical properties and fracture modes of MMS resistance spot welds

Fig. 1a shows that the paint baking at 170°C leads to the dramatic increases in both the peak load and the displacement of TS tests from 14.1 ± 0.4 to 25.7 ± 0.8 kN and 0.77 ± 0.01 to 1.33 ± 0.09 mm, respectively, i.e. both the strength and ductility of 7Mn steel weldment are almost doubled. Moreover, the peak load increases with the baking temperature (see Fig. 1b), which is in company with the linearly increasing thermal expansion (Fig. 1c), and the transition from IF to PF mode is at about 135°C, see Fig. 1d. In contrast, the nonbaked RSW nugget of 7Mn–3Cr steel exhibits the PF after the TS test (Fig. 1d). Moreover, both microhardness and nanohardness measurements reveal a low hardness zone and even some possible micropores near the centerline of nonbaked nugget, see Fig. S2.

The nonbaked 7Mn weld nugget exhibits the TS interfacial fracture (Fig. 2a), in which the crack propagates along the interface between the two welded steel sheets (Fig. 2b). The microstructure near the cracking path is martensitic dendrite (Fig. 2c). The interfacial fracture morphologies of nonbaked weld are shown in

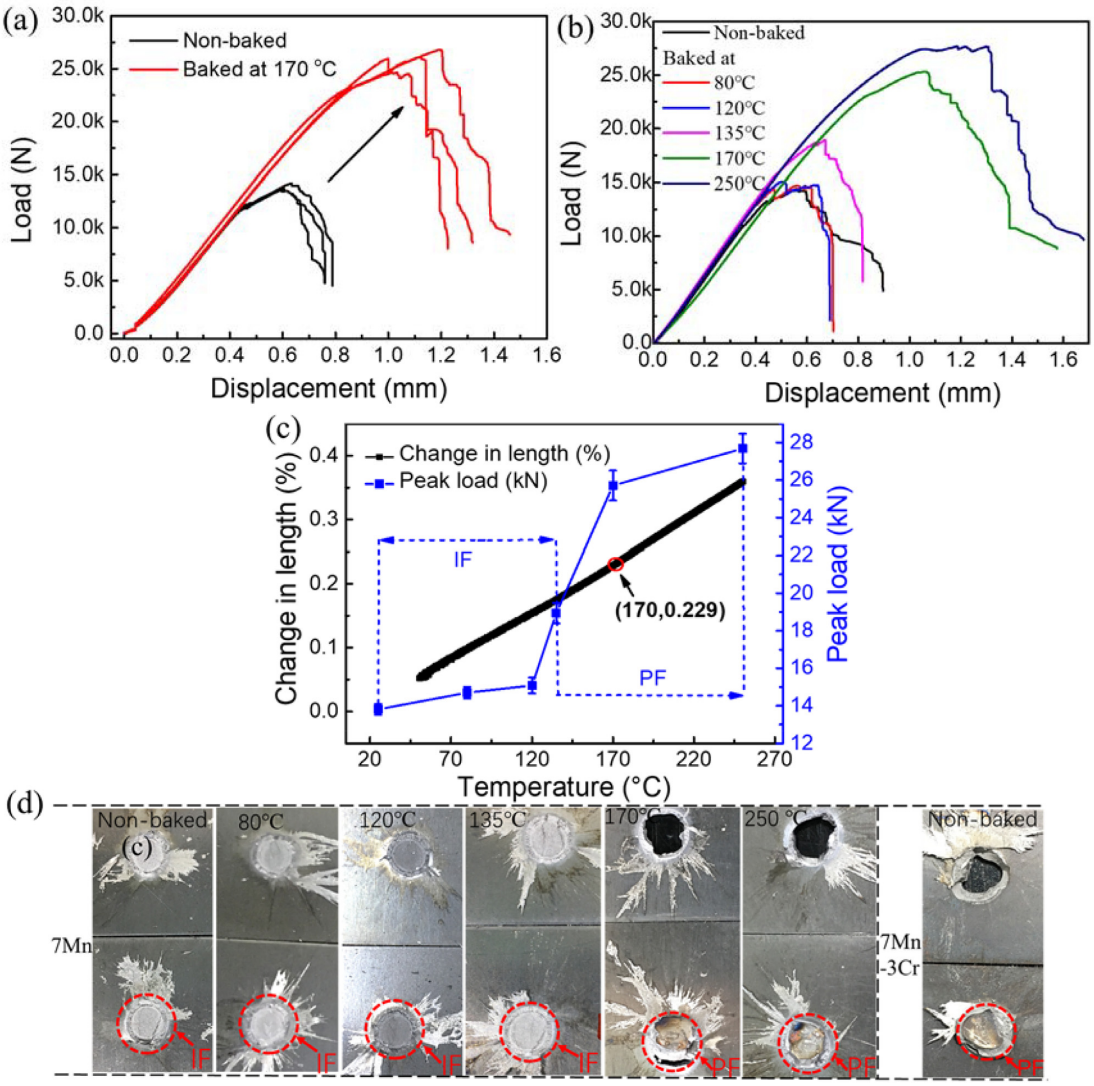

Fig. 1. Load–displacement curves of nonbaked 7Mn weldments in the TS tests compared with those baked at 170°C (a) and different temperatures for 20 min (b); the peak load, failure mode, and the measured thermal expansion of 7Mn steel nugget vary with the baking temperature (c); and the actual failure appearance for both the nonbaked 7Mn–3Cr and the 7Mn steel weldments that was baked at different temperatures (d).

Fig. 2d to f. Both the dendrites fractured along the cleavage planes and the isolated dendrites having clear tips were observed, the latter indicates that these dendrites grew from both the upper and the lower ends during solidification but did not impinge at the middle, thus leading to no joining between them and the easy initiation and propagation of crack at the nugget centerline, i.e. the IF mode in the nonbaked welds. In contrast, the 7Mn nugget baked at 170°C exhibits nearly the PF (Fig. 2g), in which the initial cracking path in martensite was along the interface but later changed to the perpendicular direction, i.e. along the growing direction of dendrite (Fig. 2h to j). Fracture morphologies along the cracking path in the baked nugget are shown in Fig. 2k and l. A mixture of both cleavage planes and dimples was observed, but no isolated dendrites with tips, suggesting much higher resistance to the interfacial cracking in the baked weld than that in the nonbaked one. Since the failure mode of either IF or PF could be affected by the cooling rate (33), the weld discontinuities, inhomogeneities and stress concentration (34), the formed discontinuities, and inhomogeneities in the unbaked MMS (see Fig. 2d and e) might contribute to the observed IF of MMS RSW weld.

Influence of paint baking on the microstructures and micro-interspaces

The microstructures near the centerlines of both the nonbaked and baked nuggets are martensitic laths, as shown in Fig. S4. It seems that there are some nanosized precipitates in the baked nugget (Fig. S4e), which however have the same atomic arrangement and lattice structure to the surrounding matrix (see Fig. S4f); thereof, they are not carbide having the mature crystal structure, but the possible clusters formed as the immature predecessor during the baking.

Fig. 3a to d shows that the dendrites in the nonbaked nugget have grown perpendicularly to the sheet surface during solidification. The full length of dendrites may be up to a half of the nugget height, i.e. 1125 μm in Fig. 3a, and many dendrites have the length more than 390 μm (Fig. 3b to d). Both the upper and lower dendrites should grow and meet at the centerline of nugget (Fig. 3c), forming an interface there. However, the micro-interspaces between the upper and lower dendrites were frequently observed near the centerline interface of nonbaked nuggets, resulting from the shrinkage during solidification, and they had the width in the

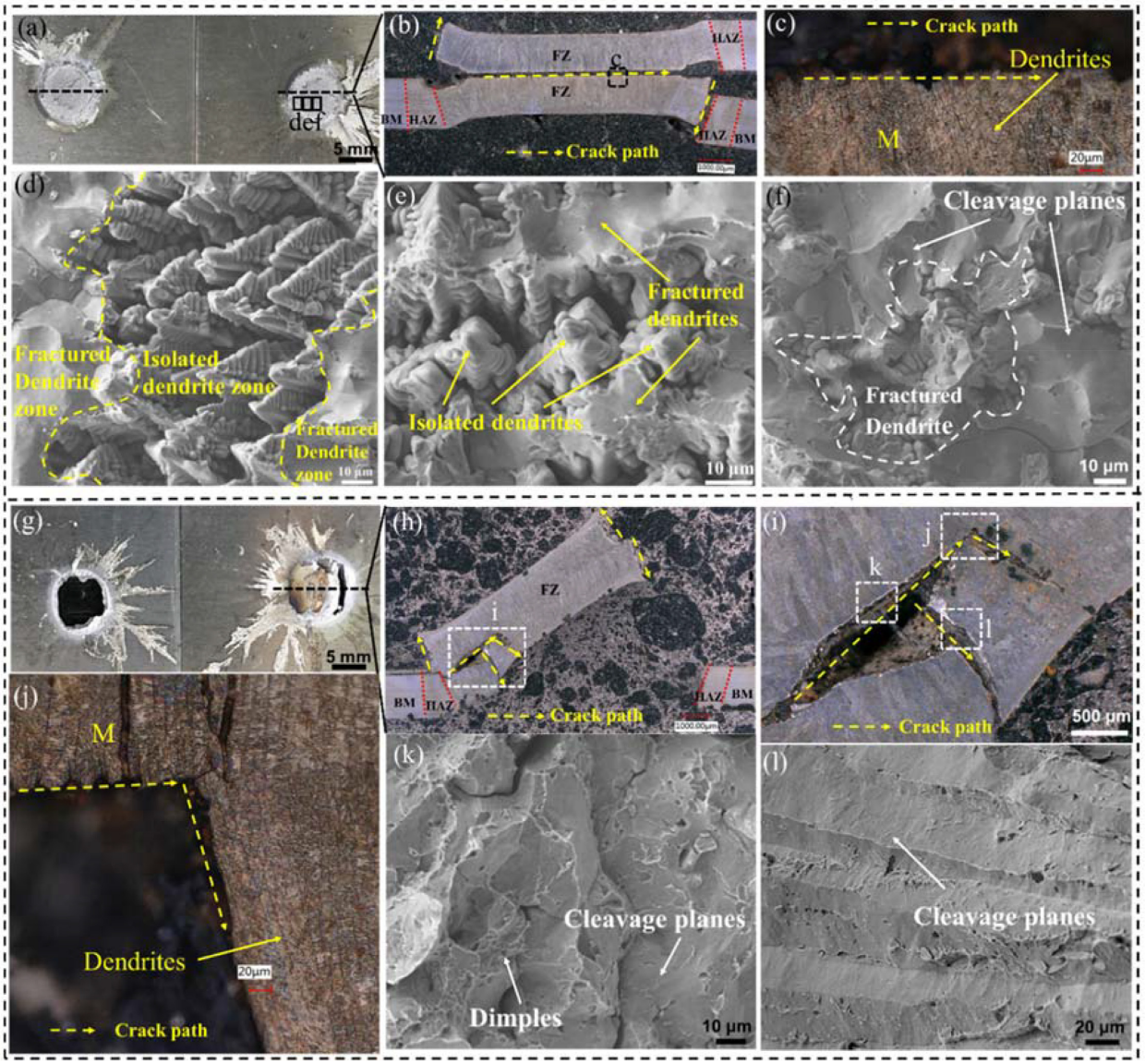

Fig. 2. IF mode of the nonbaked 7Mn steel weldment nugget (a and b); (c) the optical microstructure of the region "c" in (b); (d to f) fracture morphologies of regions "d," "e," and "f" in (a); (g and h) the PF of 7Mn steel weldment baked at 170°C; (i) the magnification of "i" in (h); (j) the optical microstructure of region "j" in (i); and (k and l) fracture morphologies of the regions "k" and "l" in (i).

range of 0.78 to 2.40 μm, see Fig. 3e to g. In contrast, much fewer and finer microvoids were found in the baked nugget (see Fig. 3f to h). Fig. 3k and l shows the statistical results on the micro-interspaces near the centerline of both the nonbaked and baked nuggets, as examined by high-resolution XCT, clearly revealing much more microvoids with the larger sizes in the nonbaked specimen than those in the baked one. These are in excellent agreement with the SEM results in Fig. 3e to j.

Discussion

Mechanism on the transition from IF to PF

The naked dendrites with the clear tips were frequently observed on the interfacial fracture surface of nonbaked specimen (Fig. 2d and e), because both the upper and lower dendrites grew toward the centerline but many of them did not impinge each other during solidification. This is because the high Mn content of studied steel can cause the great thermal contraction during solidification, which has been frequently found in Mn-alloyed steels (20, 35–37); consequently, many micro-interspaces having the size of micrometers were formed between the upper and lower dendrites (see Fig. 3e and f), leading to much reduced connection area between the two steel sheets and then the resultant IF. Although the pressure force exerted by electrodes can reduce the solidification shrinkage to some extent, it was not sufficient to press the two dendrites to be impinged. Nevertheless, the employed baking at 170°C appeared effective to eliminate these micro-interspaces so that the fracture mode changed from the IF to the PF. Both the upper and lower dendrites should expand toward the centerline during the baking until they touched each other, leading to a solid joining via so called "cold welding" mechanism, i.e. a solid joining realized without the melt of metals at the interface (38). This is often achieved under a light load at ultrahigh-vacuum environment with an atomically clean, flat, and ductile surface (39–41). For example, both gold nanowires/nanorods and PbSe nanocrystals can be cold welded well by the mechanical contact alone in the

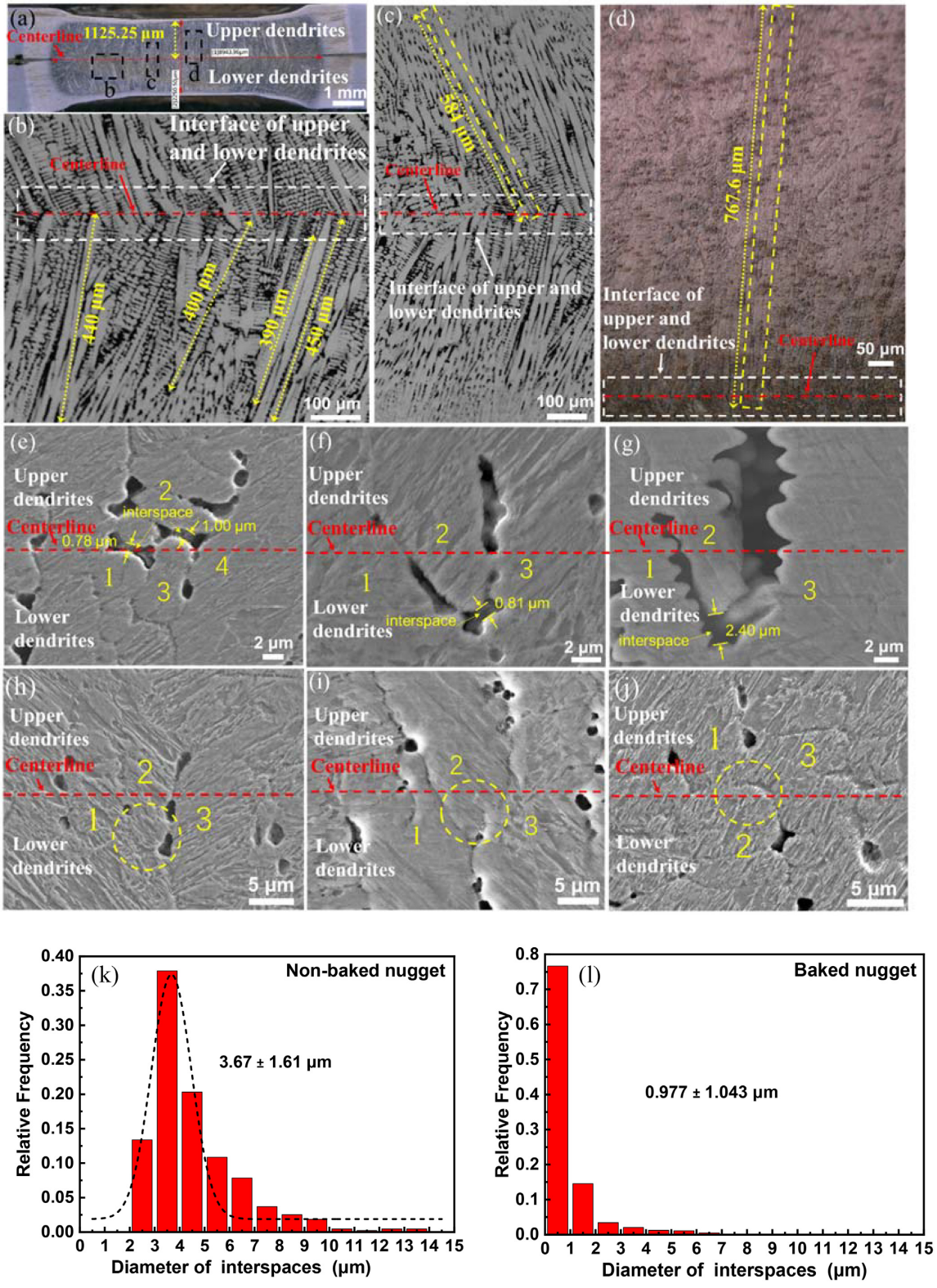

Fig. 3. Microstructure of nuggets before the tensile failure. (a) Cross-section of nonbaked nugget; (b to d) dendrite morphology of region "b to d" in (a); (e to g) microstructures with interspaces at interface of upper dendrites and lower dendrites in (b); and (h to j) microstructures without interspace at interface of upper and lower dendrites in baked nugget. 1, 2, 3, and 4: four dendrites at the centerlines of nuggets. The size distributions of interspaces near the centerline of nuggets with the average values and standard deviations are shown in for the nonbaked (k) and baked (l) specimens, examined by high-resolution XCT (also see Fig. S5 and online Videos S1 and S2 for 3D reconstruction images and animations).

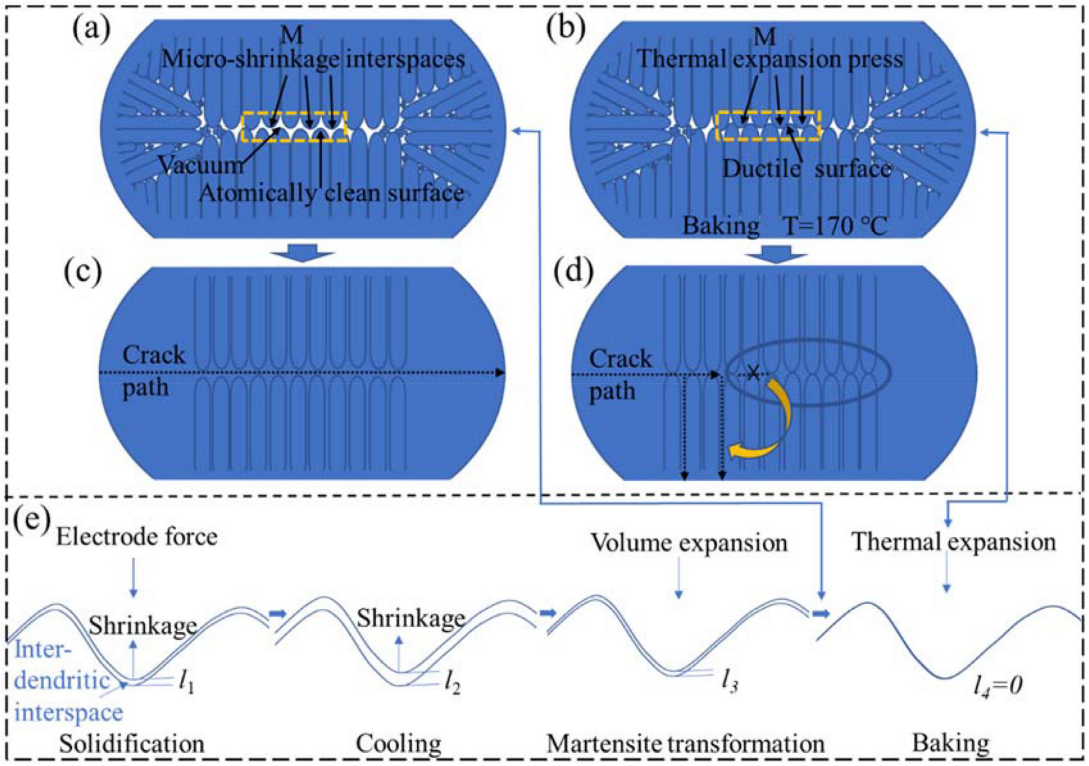

Fig. 4. The mechanism on transition from the IF to the PF of nugget due to the baking with the corresponding micro-interspaces evolving near the centerline of the nugget. Schematics on micro-interspaces in the nonbaked nugget (a) originating from solidification shrinkage and the resultant IF (c); the micro-interspaces minimized during the baking due to "cold welding" (b) and the resultant PF (d); and (e) the evolution of interdendritic micro-interspace during the welding and the baking processes.

vacuum chamber of TEM (42–44); thin gold films could be welded at remarkably low loads even under the ambient condition (41). Moreover, the as-welded zone can be as strong as the original material due to the complete connection at the interface (43). During the baking process, all these requirements for the cold welding could be satisfied. First, the closed micro-interspaces were under an ultrahigh vacuum, in which the naked dendrites had an atomically clean surface (Figs. 3d and e and 4a). Second, the baking led to the decrease of microhardness (Fig. S3a) so that dendrites became more ductile. Therefore, many naked dendrites in the upper and lower regions thermally expanded toward the centerline of nugget during the baking until they impinged each other, causing them cold welded (Fig. 4b). As a result, the bonding of two steel sheets was significantly strengthen so that the crack propagation along the interfacial path was hindered and changed to the perpendicular direction, leading to the transition of failure mode from the IF to the PF (Fig. 4c and d), and much more energy consumed during fracture. Therefore, both the peak load and displacement in the TS test increase dramatically after the baking at 170°C, see Fig. 1a. Compared with the pull-out fractured samples, there are much more interspaces in the interfacially fractured samples, and those along the centerline of nugget can be connected by deforming due to the tensile loading, leading to the IF.

The detailed mechanism is illustrated in Fig. 4e. First, the upper and lower dendrites grew toward the centerline with no impingement during welding due to the solidification shrinkage, leading to the micro-interspaces between them that cannot be fully compensated by the squeezing force exerted by the electrodes. Second, these micro-interspaces grew larger due to the further contraction of solid phases during the subsequent cooling; however, the volume expansion accompanying the martensite transformation at Ms temperature could reduce the size of micro-interspace to some extent (45). Finally, the thermal expansion during the baking caused most of isolated dendrites subjected to the mechanical contact so that the cold welding could be realized. This can be supported by a simple mathematical calculation. The lengths of solidifying dendrites are mainly in the range of 390 to 1125 μm (Fig. 3a to d) and the linear expansion of studied 7Mn steel measured at 170°C is 0.229% (Fig. 1c); thus, the thermal expansion of dendrite in the lengthwise direction during the baking was about 0.89 to 2.58 μm, which is sufficient to compensate most of the interspaces having the sizes of 0.78 to 2.4 μm in Fig. 3e to g and 3.67 ± 1.61 μm in Fig. 3k. This made the upper and lower dendrites being contacted mechanically to achieve the cold welding. A higher baking temperature than 170°C caused more dendrites cold welded due to greater expansion, resulting in the further increases of both peak load and displacement in the TS test, see Fig. 1b.

Influence of chemical composition and baking temperature

When the weldment was baked at different temperatures, a critical temperature for the transition from IF to PF at 135°C was observed. This strongly suggests that only the baking above 135°C could afford the sufficient thermal expansion to eliminate the most of micro-interspaces by making the isolated dendrites mechanically contacted for cold welding.

Such a proposed mechanism on the transition from IF to PF implies a new method of evaluating the weldability of steels, particularly for those containing high contents of alloying elements like MMS, whose weldability is not possibly assessed by CE. Instead,

we suggest that the weldability of high alloyed steels should be evaluated according to the shrinkage of nugget during both solidification and the cooling to the ambient temperature. By reasonably assuming the cooling from 1550 to 25°C during RSW at 1000°C/s (10, 19) and the primary solidified γ/δ grain size of approximate 400 μm according to Fig. 3, the values of linear contraction for the studied MMS and other AHSSs having similar alloying chemistries except for Mn content have been calculated using the commercial software JMatPro and shown in Fig. S6a. It is seen that the solidification shrinkage of 7Mn steel is largest among them apparently due to its highest Mn content. Even if the expansion accompanying austenite-to-martensite transformation is considered, the 7Mn steel still experiences the largest total shrinkage during welding. The calculated solidification shrinkages of different steel grades decrease in the sequence of 7Mn, 5Mn to MS1400, which corresponds very well to the IF of 7Mn, the PIF of 5Mn, and the PF of DP980, MS1200, and MS1400 steel grades (see Fig. S6b). Moreover, the observed PIF for 5Mn steel weld nugget suggests that the Δl of 5Mn is a threshold value for the transition from IF to PF mode. This implies a new criterion on assessing weldability of high-alloyed steels like MMS.

New shrinkage-based criterion (Δl) for evaluating weldability

Today, the weldability of steels is most widely evaluated by the formulas of CE, proposed by the International Institute of Welding (IIW) (46) and American Welding Society (AWS) D1.1 (46), as follows:

$$CE_{IIW} = C + (Mn/6) + (Cr + Mo + V)/5 + (Ni + Cu)/15\ (wt.\%), \quad (1)$$

$$CE_{AWSD1.1} = C + (Mn + Si)/6 + (Cr + Mo + V)/5 + (Ni + Cu)/15\ (wt.\%). \quad (2)$$

However, these formulas are just the empirical formula derived from the accumulated engineering experience and lack of the clear physical background; thereof, it faces the increasing difficulty in accurately assessing the weldability of high alloyed steels. We calculated the CE values for a wide range of typical AHSSs by Eq. 1 and plotted them together with the corresponding fracture modes of RSW in Fig. 5a. When the total alloying contents excluding C element are more than 2 wt.%, most of CE values are greater than 0.4% and the IF mode starts to appear. However, both PF and IF modes appear when CE values are in the range of 0.4% to 0.6%, where the superior weldability of DP780/980, PHS22MnB5, TRIP980, and CP1100 steel grades cannot be distinguished from the inferior weldability of QP980 and TRIP800. Furthermore, both a TWIP 980 and the 7Mn–3Cr steels exhibit superior weldability with the PF mode although their CE values are very high.

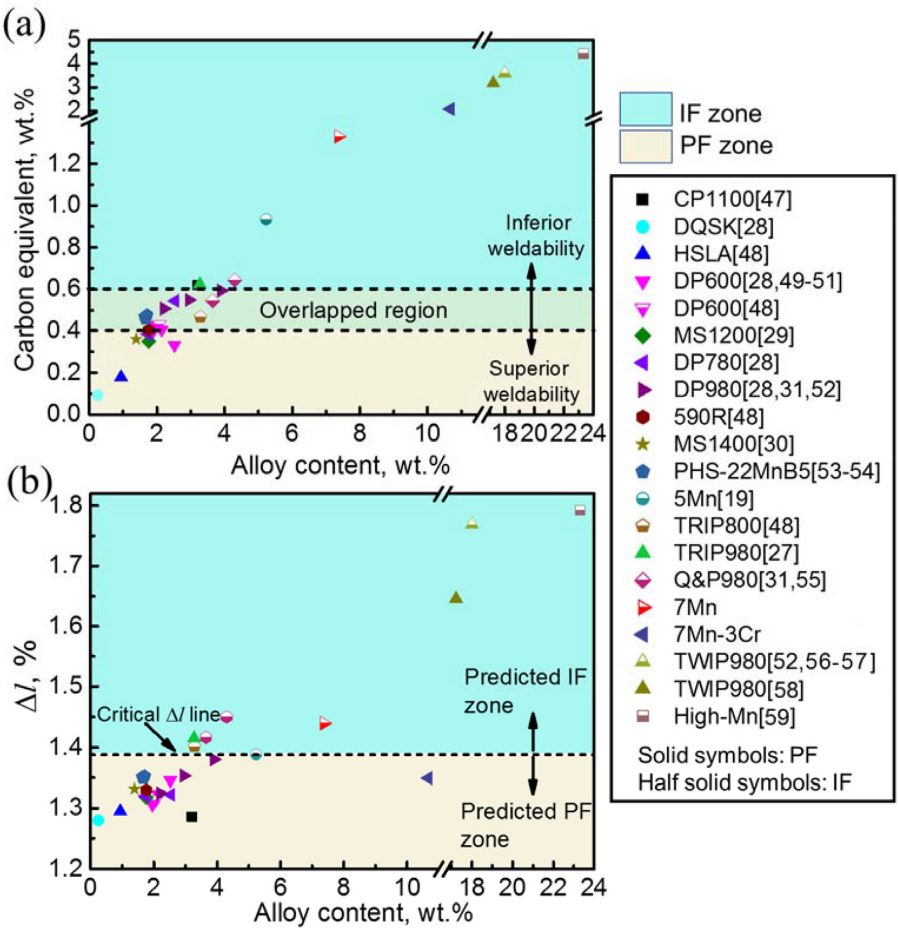

Fig. 5. CE (a) and Δl (b) values of selected AHSSs and MMSs calculated by Eqs. 1 from Refs. (19, 27–31, 47–55) and 4, from Refs. (19, 27–31, 47–59) respectively, together with the corresponding fracture mode of RSW nugget in TS test. Alloy content is the sum of weight percentages of all the elements included in these equations except for C.

To solve this problem, we propose a new criterion on the clear physics, i.e. the shrinkage of weldment, which can be calculated by the following procedures. First, the influence of each individual alloying element with a usual range on the solidification shrinkage of steel (Δl) during welding was calculated using the commercial software JMatPro 12.4. The calculations assume that the steel melt is cooled from 1550°C at the rate of 1000°C/s during welding (17, 20) and the solidified grain size 400 μm (see Fig. 3). The calculated results are given in Fig. S7a to c. About 80 sets of data points were calculated for the eight most common alloying elements that are included in the CE equations. These data were then fitted by the following multiple linear regression to derive the relationship between the weight percentage of alloying element i (x_i) and the resultant solidification shrinkage (Δl) (60):

$$\Delta l = \alpha_0 + \sum_{i=1}^{n} \alpha_i x_i. \quad (3)$$

The coefficients of α_0 and α_i were determined by the least square fitting for each element and then summarized in Table S1 together with its best valid range, finally leading to the following equation:

$$\begin{aligned}\Delta l = {} & 1.259 + 0.301x_C + 0.0183x_{Mn} - 0.0359x_{Cr} \\ & - 0.0153x_{Ni} - 0.00556x_{Mo} + 0.0354x_{Si} \\ & + 0.0168x_{Cu} - 0.118x_V. \end{aligned} \quad (4)$$

The values of correlation coefficient R^2, significance F, and P are summarized in Table S1, indicating that the multiple linear regression analysis is valid and sufficiently accurate (60, 61), and the discrepancy between the results calculated using Eq. 4 and the commercial JMatPro is less than 3%, see Fig. S7d.

To examine the robustness of the proposed Eq. 4 on assessing weldability, we plot all the calculated Δl values together with the TS fractured modes in Fig. 5b for the same weldments of steel grades in Fig. 5a. The calculated Δl value of 5Mn steel, 1.39%, is set as the critical value due to its partial IF mode. Almost all the welds of studied steels exhibit the IF mode when $\Delta l > 1.39\%$ and the PF when $\Delta l < 1.39\%$ except for just a few exceptions, the latter may result from other factors that can affect the solidification shrinkage to some extent. For example, the thickness of steel sheets (46, 50) and the bare or coated surface (47) can also influence the cooling rate after welding. Note that the Δl value of 7Mn–3Cr steel is 1.35%, lower than both the critical value of 1.39% and the Δl of 7Mn steel, primarily because the addition of 3% Cr could reduce the solidifying shrinkage according to Eq. 4. This correctly predicts that 7Mn–3Cr steel exhibits the PF mode with a good weldability (see Fig. 1d) despite of its high CE value of 2.08%. This demonstrates that our proposed Δl criterion can be used to evaluate and even predict the weldability of alloyed steels more accurately and robustly than the classic CE concept.

Although the proposed Eq. 4 is just for quantifying the shrinkage of weldment, the calculated result could represent the shrinkage of heat affected zone (HAZ) to some extent too since the influences of these alloying elements on the shrinkages of both HAZ and weldment are similar. Greater shrinkage always causes higher internal stress generated after cooling. The classical CE approach is actually to assess the tendency of hydrogen-induced cracking in HAZ, which is directly related to stress level (10). In contrast, our proposed Δl criterion has the capability of quantifying the tendency of cracking in both zones; therefore, it can be used to evaluate the weldability of alloyed steels more accurately and robustly than the present CE concept.

Conclusion

In this paper, we investigated why the RSW nuggets in 7Mn and 7Mn–3Cr steels exhibited the IF and PF, respectively, when they were subjected to the TS test, and the baking of 7Mn at no less than 170°C led to the TS fracture mode from the IF to the PF. The following conclusions can be drawn.

(1) The RSW nugget of 7Mn steel, like many MMSs, exhibited the typical IF during the TS test because the high Mn content led to sufficiently great solidification shrinkage during welding. Consequently, many micro-interspaces were formed between the upper and lower dendrites without impingement; in contrast, the solidification shrinkage of 7Mn–3Cr steel during welding was remarkably reduced due to the addition of 3% Cr, resulting in PF in the TS test.
(2) The baking at no less than 170°C can afford a sufficient thermal dilatation so that most of unimpinged dendrites in 7Mn steel were mechanically contacted for achieving the "cold welding," leading to the transition of TS fracture mode from the IF to the PF with improved mechanical property.
(3) We establish a new model on calculating the total shrinkage during welding merely from the chemical compositions, by which the criterion $\Delta l > 1.39\%$ predicts the IF mode of RSW during the TS test otherwise the PF mode for $\Delta l < 1.39\%$. The calculated results by both Δl and CE approaches were compared with the observed fracture modes, which indicates that the former can assess the weldability of greater range of AHSS more accurately and robustly than the latter, particularly for the high alloyed steels. Moreover, it is expected that this model could be extended from RSW to other welding processes, such as laser or arc welding, since they all share the similar metallurgical phenomena like heat input/transfer, melting, and solidification. Therefore, it is promising to replace CE in all the relevant engineering circumstances in future.

Supplementary Material

Supplementary material is available at *PNAS Nexus* online.

Funding

H.W.L. gratefully acknowledges the financial supports from the National Natural Science Foundation of China (No. 51831002) and the Fundamental Research Funds for the Central Universities (No. FRF-TP-18–002C2). S.L.Y. is grateful to the Shanghai Municipal Economic and Informatization Commission (No. GYQJ-2019–1–33), the Science and Technology Commission of Shanghai Municipality (No. 19XD1433500), and the National Natural Science Foundation of China (No. 51861024).

Authors' Contributions

S.S.L. did most of experimental works and wrote the first draft; Y.J.W. and W.T. did some welding tests; B.H. did some microstructural characterization; S.L.Y. supervised welding tests and revised manuscript; and H.L.W. designed and supervised project and revised manuscript.

Data Availability

All data are included in the manuscript and/or supporting information.

References

1. Xie ZJ, *et al.* 2018. A novel multi-step intercritical heat treatment induces multi-phase microstructure with ultra-low yield ratio and high ductility in advanced high-strength steel. Scr Mater. 155:164–168.
2. Ashiri R, *et al.* 2015. Supercritical area and critical nugget diameter for liquid metal embrittlement of Zn-coated twining induced plasticity steels. Scr Mater. 109:6–10.
3. Ashiri R, *et al.* 2016. Liquid metal embrittlement-free welds of Zn-coated twining induced plasticity steels. Scr Mater. 114:41–47.
4. Ashiri R, Mostaan H, Park YD. 2018. A phenomenological study of weld discontinuities and defects in resistance spot welding of advanced high strength TRIP steel. Metall Mater Trans A. 49:6161–6172.
5. Ahsan MRU, *et al.* 2016. Porosity formation mechanisms in cold metal transfer (CMT) gas metal arc welding (GMAW) of zinc coated steels. Sci Technol Weld Join. 21:209–215.
6. Ahsan MRU, *et al.* 2016. Cold metal transfer (CMT) GMAW of zinc-coated steel. Weld J. 95:120–132.
7. Ahsan MRU, *et al.* 2017. Mechanisms of weld pool flow and slag formation location in cold metal transfer (CMT) gas metal arc welding (GMAW). Weld World. 61:1275–1285.
8. Yang S, Carlson B, Kovacevic R. 2011. Laser welding of high-strength galvanized steels in a gap-free lap joint configuration under different shielding conditions. Weld J. 90:8/s–18/s.
9. Yang S, Kovacevic R. 2009. Welding of galvanized dual-phase steels in a gap-free lap joint configuration under different shielding conditions. Weld J. 88:168/s–178/s.
10. Krajcarz F, Gourgues-Lorenzon AF, Lucas E. 2016. Influence of carbon content on the primary solidification mode of high strength steels in resistance spot welding conditions. Scr Mater. 120:98–102.
11. Sun X, Stephens EV, Khaleel MA. 2007. Effects of fusion zone size and failure mode on peak load and energy absorption of advanced high-strength steel spot welds. Weld J. 86:18–25.
12. Li X, Song R, Zhou N, Li J. 2018. An ultrahigh strength and enhanced ductility cold-rolled medium-Mn steel treated by intercritical annealing. Scr Mater. 154:30–33.
13. Liu L, *et al.* 2020. Making ultrastrong steel tough by grain-boundary delamination. Science. 368:1347–1352.
14. He BB, *et al.* 2017. High dislocation density–induced large ductility in deformed and partitioned steels. Science. 357: 1029–1032.
15. Han J, *et al.* 2017. Superplasticity in a lean Fe–Mn–Al steel. Nat Commun. 8:1–6.
16. Ding R, *et al.* 2020. Chemical boundary engineering: a new route toward lean, ultrastrong yet ductile steels. Sci Adv. 6:eaay1430.
17. Li SS, *et al.* 2021. A novel medium-Mn steel with superior mechanical properties and marginal oxidization after press hardening. Acta Mater. 205:116567.
18. Park G, Jeong S, Lee C. 2020. Fusion weldabilities of advanced high manganese steels: a review. Met Mat Int. 27:1–13.
19. Jia Q, *et al.* 2018. Microstructure and tensile-shear properties of resistance spot-welded medium Mn steel. Metals. 8:1–13.
20. Li SS, *et al.* 2019. A novel shim-assisted resistance spot welding process to improve weldability of medium-Mn transformation-induced plasticity steel. Metall Mater Trans B. 50:1–9.
21. Park G, Kim K, Uhm S, Lee C. 2019. A comparison of cross-tension properties and failure behavior between similar and dissimilar resistance spot-weldments in medium-Mn TRIP steel. Mater Sci Eng A. 752:206–216.
22. Sun X, Stephens EV, Khaleel MA. 2008. Effects of fusion zone size and failure mode on peak load and energy absorption of advanced high strength steel spot welds under lap shear loading conditions. Eng Fail Anal. 15:356–367.
23. Ashiri R, Marashi SPH, Park YD. 2018. Weld processing and mechanical responses of 1-GPa TRIP steel resistance spot welds. Weld J. 97:157–169.
24. Park G, Kim K, Uhm S, Lee C. 2019. Remarkable improvement in resistance spot weldability of medium-Mn TRIP steel by paint-baking heat treatment. Mater Sci Eng A. 766:138401.
25. Wang Y, *et al.* 2020. Effect of the cooling time on the cross tensile strength of the resistance spot welded medium manganese steel. In TMS 2020 149th Annual Meeting and Exhibition Supplemental Proceedings. Springer, Cham. 515–523.
26. Wang Y, *et al.* 2020. Highly enhanced cross tensile strength of the resistance spot welded medium manganese steel by optimized post-heating pulse. In The Minerals, Metals and Materials Society TMS 2020 149th Annual Meeting and Exhibition Supplemental Proceedings. The Minerals, Metals and Materials Series. Springer, Cham. 1871–1880.
27. Cho H, *et al.* 2019. Fatigue behaviors of resistance spot welds for 980 MPa grade TRIP steel. Metals. 9:1086.
28. Pouranvari M, Marashi SPH, Safanama DS. 2011. Failure mode transition in AHSS resistance spot welds, part II: experimental investigation and model validation. Mater Sci Eng A. 528:8344–8352.
29. Pouranvari M, Sobhani S, Goodarzi F. 2018. Resistance spot welding of MS1200 martensitic advanced high strength steel: microstructure-properties relationship. J Manuf Process. 31:867–874.
30. Tamizi M, Pouranvari M, Movahedi M. 2017. Welding metallurgy of martensitic advanced high strength steels during resistance spot welding. Sci Technol Weld Join. 22:327–335.
31. Shamsujjoha M, Enloe CM, Chuang AC, Coryell JJ, Ghassemi-Armaki H. 2021. Mechanisms of paint bake response in resistance spot-welded first and third generation AHSS. Materialia. 15:100975.
32. Vander Voort GF. 1984. Metallography: principles and practice. Materials Park (OH): ASM International. p. 213–214. ISBN: 0-87170-672-5.
33. Ashiri R, Marashi SPH, Park YD. 2018. Weld processing and mechanical responses of 1-GPa TRIP steel resistance spot welds. Weld J. 97:157/s–169/s.
34. Beni SS, Atapour M, Salmani MR, Ashiri R. 2019. Resistance spot welding metallurgy of thin sheets of zinc-coated interstitial-free steel. Metall and Mat Trans A. 50:2218–2234.
35. Xie HJ, Wu XC, Min YA. 2008. Influence of chemical composition on phase transformation temperature and thermal expansion coefficient of hot work die steel. J Iron Steel Res Int. 15:56–61.
36. Hull FC, Hwang SK, Wells JM, Jaffee RI. 1987. Effect of composition on thermal expansion of alloys used in power generation. J Mater Eng. 9:81–92.
37. Hwang SK, Hull FC, Wells JM. 1984. Effects of the alloying elements on the thermal expansion coefficient of nonmagnetic Ni-base alloys and austenitic steels. Paper presented at: Fifth International Symposium on Superalloys; Seven Springs (PA), USA. pp. 785–794.
38. Freitas RA, Gilbreath WP. 1980. Advanced automation for space missions. Paper presented at: Proceedings of the 1980 NASA/ASEE Summer Study, Appendix 4C.1. (NASA).
39. Jellison JL, Zanner FJ. 1983. Modern methods for cold welding: metals handbook. 9th ed. Metals Park (OH): American Society for Metals. p. 672.

40. Tabor D, Blakely JM. 1975. Surface physics of materials. New York (NY): Academic Press. p. 475–529.
41. Ferguson GS, Chaudhury MK, Sigal GB, Whitesides GM. 1991. Contact adhesion of thin gold films on elastomeric supports: cold welding under ambient conditions. Science. 253:776–778.
42. Van Huis MA, *et al*. 2008. Low-temperature nanocrystal unification through rotations and relaxations probed by in situ transmission electron microscopy. Nano Lett. 8:3959–3963.
43. Lu Y, Huang JY, Wang C, Sun S, Lou J. 2010. Cold welding of ultrathin gold nanowires. Nat Nanotechnol. 5:218–224.
44. Dai G, Wang B, Xu S, Lu Y, Shen Y. 2016. Side-to-side cold welding for controllable nanogap formation from "dumbbell" ultrathin gold nanorods. ACS Appl Mater Interfaces. 8:13506–13511.
45. Moyer JM, Ansell GS. 1975. The volume expansion accompanying the martensite transformation in iron–carbon alloys. Metall Trans A. 6:1785.
46. Talaş Ş. 2010. The assessment of carbon equivalent formulas in predicting the properties of steel weld metals. Mater Design. 31:2649–2653.
47. Kong JP, Han TK, Chin KG, Park BG, Kang CY. 2014. Effect of boron content and welding current on the mechanical properties of electrical resistance spot welds in complex-phase steels. Mater Design. 54:598–609.
48. Khan MI. 2007. Spot welding of advanced high strength steels (AHSS) [master's thesis]. Waterloo (ON): University of Waterloo.
49. Marya M, Wang K, Hector LG, Jr, Gayden X. 2006. Tensile-shear forces and fracture modes in single and multiple weld specimens in dual-phase steels. J Manuf Sci Eng. 128: 287–298.
50. Wan X, Wang Y, Zhang P. 2014. Effects of welding schedules on resistance spot welding of DP600 steel. ISIJ Int. 54:2375–2379.
51. Yang H, Zhang Y, Lai X, Chen G. 2008. An experimental investigation on critical specimen sizes of high strength steels DP600 in resistance spot welding. Mater Design. 29:1679–1684.
52. Yu J, Shim J, Rhee S. 2012. Characteristics of resistance spot welding for 1 GPa grade twin induced plasticity steel. Mater Trans. 53:2011–2018.
53. Ighodaro EB, Zhou YN. 2016. Comparative effects of Al-Si and galvannealed coatings on the properties of resistance spot welded hot stamping steel joints. J Mater Process Technol. 236:64–72.
54. Han X, Razmpoosh MH, Macwan A, Biro E, Zhou Y. 2020. Effect of galvannealed coating evolution during press hardening on RSW weldability. Weld J. 99:156–162.
55. Liu XD, *et al*. 2019. Mechanical properties in double pulse resistance spot welding of Q&P 980 steel. J Mater Process Tech. 263:186–197.
56. Saha DC, Cho Y, Park YD. 2013. Metallographic and fracture characteristics of resistance spot welded TWIP steels. Sci Technol Weld Join. 18:711–720.
57. Saha DC, Han S, Chin KG, Choi I, Park YD. 2012. Weldability evaluation and microstructure analysis of resistance-spot-welded high-Mn steel in automotive application. Steel Res Int. 83:352–357.
58. Tutar M, Aydin H, Bayram A. 2017. Effect of weld current on the microstructure and mechanical properties of a resistance spot-welded TWIP steel sheet. Metals. 7:519.
59. Russo Spena P, De Maddis M, Lombardi F, Rossini M. 2015. Investigation on resistance spot welding of TWIP steel sheets. Steel Res Int. 86:1480–1489.
60. Placca L, Kouta R, Candusso D, Blachot JF, Charon W. 2010. Analysis of PEM fuel cell experimental data using principal component analysis and multi linear regression. Int J Hydrog Energy. 35:4582–4591.
61. Záhumenský P, Kohútek I, Semeňák J. 2017. Austenite–ferrite transformation temperature regression equations for low carbon steels with cooling rate account. IOP Conf Ser Mater Sci Eng. 283:012024.